Terra Nova

Neogene exhumation history of the Bergell massif (southeast Central Alps).

Journal:	*Terra Nova*
Manuscript ID:	TER-2012-0025.R2
Wiley - Manuscript type:	Paper
Date Submitted by the Author:	n/a
Complete List of Authors:	Mahéo, Gweltaz; LGTE UMR 5276 - CNRS, UCB Lyon1 - ENS Lyon Gautheron, Cécile; UMR Interactions et Dynamique des Environnements de Surface – CNRS-UPS 814, Université Paris Sud Leloup, Philippe-Hervé; LGTE UMR 5276 - CNRS, UCB Lyon1 - ENS Lyon Fox, Matthew; ETH Zürich, Geologisches Institut Tassant-Got, Laurent; Institut de Physique Nucléaire, CNRS/IN2P3, Université Paris Sud Douville, Eric; Laboratoire des Sciences du Climat et de l'Environnement - UMR 8212 CNRS-CEA-UVSQ,
Keywords:	Alps, Miocene, Extrusion, He thermochonology, 1D thermal modeling

Neogene exhumation history of the Bergell massif (southeast Central Alps).

Gweltaz Mahéo[1], Cécile Gautheron[2], Philippe-Hervé Leloup[1], Matthew Fox[3], Laurent Tassant-Got[4] and Eric Douville[5]

1- Laboratoire de Science de la Terre, CNRS-UMR5570, Université Claude Bernard Lyon1, ENS Lyon, Université de Lyon, 69100 Villeurbanne, France, gweltaz.maheo@univ-lyon1.fr, phone : + 33 4 72 44 52 36

2- UMR Interactions et Dynamique des Environnements de Surface – CNRS-UPS 8148, Université Paris Sud, 91405 Orsay, France

3- ETH Zürich, Geologisches Institut, NO E49, Sonneggstr. 58092 Zurich, Switzerland

4- Institut de Physique Nucléaire, CNRS/IN_2P_3, Université Paris Sud, 91405 Orsay, France,

5- Laboratoire des Sciences du Climat et de l'Environnement - CNRS, Giff/Yvette, France

Running head : Bergell massif exhumation history

ABSTRACT

The Bergell pluton is an elongated plutonic body emplaced during Oligocene time along the Insubric line in the central Alps. Reconstruction of its exhumation based on apatite (U-Th)/He dating and one dimension thermal modeling, provide evidence for a three steps history: (1) following initial fast exhumation from >20-25 to ~17 Ma, slow down of the exhumation rate until ~10 Ma, (2) quiescent phase from ~10 to ~5-6 Ma and (3) an apparent increase of exhumation after ~5-6 Ma. The decrease of exhumation rate is related with migration of thrusting south of the Bergell area in the Southern Alps (Lombardic phase). Increase in exhumation rate after ~5-6 Ma is possibly related with Messinian base level drop, enhanced climatic variability (3-4 Ma) and intensification of glaciation (~0.87 Ma).

INTRODUCTION AND GEOLOGICAL SETTING

Accommodation of intra-continental convergence by the combination of shortening and lateral escape has been proposed for several mountain ranges such as the Himalayan-Tibet system (Tapponnier et al., 1986), or the Alps (Ratschbacher et al., 1991). In the Alps, lateral escape initiated in the Oligocene due to the northward indentation of the Adriatic plate in the Austro-alpine Penninic wedge (Ratschbacher et al., 1991; Schmid et al., 1996). To further understand the alpine tectonic evolution during indentation, and its interaction with external factors, we reconstructed the Neogene exhumation history of the Bergell pluton located along the Tonale fault, one of the major faults accommodating the eastward extrusion. The study is based on eleven new apatite (U-Th)/He (AHe) ages of samples collected along two horizontal and one vertical profile within the Bergell massif.

The Bergell massif mainly consists of a granodioritic and tonalitic pluton emplaced 31-28 Ma (Oberli et al., 2004) within the Penninic nappes along the insubric mylonitic belt (Rosenberg et al., 1995, Fig. 1b). After nappes stacking, High-Pressure metamorphism was overprinted by a barrovian metamorphism event. Thermal peak was reached between 28 and 21 Ma (Engi et al., 2004), and followed by rapid cooling until ~16 Ma (Hurford, 1986). The northern edge of the Bergell massif corresponds to the SW end of the NE-SW trending, sinistral strike slip Engadine Line. The massif is framed by two NW-SE striking top to the SW normal faults, the Forcola Line to the west and the Muretto fault to the east (e.g. Ciancaleoni & Marquer, 2008, Fig. 1). In this area major post intrusion tectonic episodes are related with the northward indentation of the Penninic zone by the Adriatic upper crust (Ratschbacher et al., 1991; Zwingmann & Mancktelow, 2004; Ciancaleoni & Marquer, 2008). Indentation first induced folding and backthrusting as well as eastward horizontal extrusion (32-25 Ma)

accommodated by ductile conjugate transpressive strike-slip motion along the Insubric mylonitic belt and the Engadine line, respectively. The extrusion then continued between 25 and 17 Ma by displacement along the Engadine Line and the dextral strike-slip Tonale fault, the latter being parallel to the Insubric mylonitic belt. This extrusion is associated with orogen parallel extension along the Forcola Line and the Muretto fault (Ciancaleoni & Marquer, 2008).

(U-TH)/HE DATING AND MODELING

AHe ages (Table 1) were obtained from (1) a constant elevation (~1000 m) E-W trending profile along and north of the Tonale Fault (Fig. 1), (2) a constant elevation (~1100 m), N-S trending profile across the Tonale Fault (Fig. 2a), and (3) a nearly vertical profile (1020-3140 m) in the core of the Bergell pluton (Figs 1, 2 and 3). For each sample, two to five replicates using inclusion free grains were measured and placed into a platinum basket. Alpha-ejection factors have been determined following Gautheron et al. (2006) (Table 1). The platinum basket was heated twice at 1030±50°C for 5 minutes using a diode laser, allowing the total degassing of He. The second heating allows testing if He-rich inclusions are present (monazite, zircon). The ^{4}He content (Table 1) has been determined by comparison with a 3-4×10^{-7} ccSTP ^{3}He spike procedure, following Farley (2002) at the University Paris-sud He lab. Apatite were then dissolved with a 50 µl solution of HNO_3 containing a known content of ^{235}U and ^{230}Th during at least one hour at 90°C. After adding 1 ml of miliQ water, U and Th content (table 1) was determined using the ICP-MS equipment of the LSCE (Giff/Yvette; France) following Evans et al. (2005). The ^{235}U and ^{230}Th of the final solution are close to 0.2 ppb. Durango and Limberg tuff apatite together with our samples yielded ages of 30.5±2.2 and 16.7±1.3Ma respectively, in agreement with literature data (McDowell, et al., 2005, Kraml, et al., 2006). SEM analysis carried out at University Paris-sud, on grains similar to the ones that have been analyzed, do not evidence any significant U or Th zoning nor the presence of any inclusions (Fig. 4).

Most AHe ages between replicates are identical within error; except two replicates (BG17-D and BG21-B) that were excluded from the mean calculation (Table 1). The lack of correlation between age and U content shows that alpha-recoil damage does not have a significant effect on He diffusion (Gautheron et al., 2009) and standard He diffusion of Farley (2000) can be used for modelling. No significant AHe age variation is observed along the E-W horizontal profile (Fig. 1), with ages ranging from 8.5±1.0 to 11.5±2.0 Ma (Fig. 1b). Along the N-S near horizontal profile, AHe ages exhibit a negative correlation with the swath profile topography, the oldest ages (9.5-11.5 Ma) being located close to the Valtellina valley (Fig. 2a) and the younger

ages further south and north (5.8±0.5, 5.4±0.3 Ma respectively). AHe ages from the Bergell vertical profile span from 5.4±0.4 to 16.2±1.0 Ma. When plotted as age versus elevation (Fig. 3) these ages define two apparent exhumation rates: ~0.9 km/Myr between 16.2 and 15.0 Ma and ~0.11 km/Myr (r^2=0.97) between 15.0 and 5.4 Ma. The first exhumation rate is less reliable because it is based on only two data. Nearby apatite fission track (AFT) ages (Fig. 1b) range from 16.8 to 8.1 Ma (Wagner et al., 1977; 1979), and define a single apparent exhumation rate of ~0.37 km/Myr (r^2=0.97) (Fig. 3). This rate appears lower than the one obtained from the two oldest AHe ages (0.9 km/Myr). However, this discrepancy is not significant as the AHe rate is based on only two data with relatively high uncertainties (Fig. 3).

To quantify the exhumation history, AHe and AFT ages have been analyzed using a linear inverse approach (Fox et al., in prep). A one-dimensional thermal model, including the effects of advection due to erosion, is used to estimate the closure depths at the time corresponding to the ages of each dated sample following Dodson (1973), and AHe diffusion coefficient (Farley, 2000) or AFT annealing parameters (Ketcham et al., 2007). The estimated closure depths are corrected to account for the perturbation of temperature in the crust due to topography using a spectral method (Mancktelow & Grasemann, 1997; Fellin et al., 2007; Thomson et al., 2010). The total time simulated is from 25 Ma to the present day and exhumation rate is piecewise constant over time intervals of 3-5 Myr, depending on the model. First, a prior exhumation rate (PER) is used to calculate the one-dimensional thermal model. Then for each time interval, exhumation rates are derived by regressing a weighted piecewise linear line through a stacked pseudo-Age Elevation Relationship (pseudo-AER, Reiners et al., 2003), derived from a measured age against calculated closure depth plot. In time intervals where the number of data is insufficient to estimate the exhumation rate, the prior rate is used (this is the case during the earliest history). This pseudo-AER accounts for differences in the thermochronometric system, advection of heat due to erosion and the perturbation of closure depths due to topography. The regression is weighted with respect to the measurement uncertainty of the age and the fixed uncertainty of the prior model (PER +/- 0.15). The sensitivity of the model to changes in the prior model is discussed below. Then, for the investigated time interval, the one-dimensional thermal model is updated using the estimated exhumation. The closure depths are recalculated and a new exhumation rate derived from the updated pseudo-AER. This process is iterated until the model converges, usually 3 or 4 times. Finally the uncertainty of the exhumation rate estimate (grey envelope on Fig. 5) is calculated following (Tarantola (2005). For the last time interval, a mean exhumation rate is calculated between the estimated present day and our youngest sample closure isotherms depth. Consequently, as no ages younger than 5 Ma have been measured, the modeled exhumation rate since 5 Ma is only controlled by the

predicted closure depth of the youngest age, which is based on the thermal model.

Models were calculated for PER's between 1 and 0.3 km/Myr and initial geothermal gradients from 16 to 38°C/km. The misfit to the data is quantified following Braun and Robert (2005). In all simulations the final misfit is an order of magnitude less than the misfit calculated with the PER for each time interval (constant exhumation rate reference model, or prior model), showing that a change in exhumation is required. While a large range of solutions are produced, the simulations that show low misfits (≤ 2.4) share first order characteristics, with exhumation rate decreasing around 10 Ma and increasing after 6 Ma (Fig. 5). The lowest misfits (1.6-1.7) are obtained for prior exhumation rates of 0.3 to 0.5 km/Myr and suggest that exhumation rate decreases around 15 Ma and again around 10 Ma (Fig. 5 A, B, E, F). However, a progressive exhumation rate decrease from ~15 to ~10 Ma cannot be ruled out as we have discretized the exhumation history over this time interval.

DISCUSSION

Lack of AHe age variation along the E-W constant elevation profile suggests that no significant eastward or westward tilting has taken place since ~10 Ma. The Bergell has been tilted by 11° towards the east (Rosenberg & Heller, 1997) and our results are compatible with the age proposed for the cessation of this tilting at 13 Ma (Villa & von Blankenburg, 1991; Rosenberg & Heller, 1997). The negative correlation between AHe ages and topography along the N-S nearly horizontal profile (Fig. 2a), could be related to higher exhumation rates on both sides of the valley, for which there is no tectonic evidence. This correlation is more probably related to the deflection by the topography of the ~70°C isotherm or topographic change between ~10 and ~5 Ma. Considering the slow (~0.1 km/Myr) apparent exhumation rate deduced from the vertical profile in this time interval, the observed ~5 Ma age difference could result from a ~500 m negative perturbation of the AHe closure isotherm below the valley. Such a deflection is compatible with a ~2500 m deep, ~20km wavelength valley comparable to that of today (Stüwe et al., 1994; Braun, 2002). This would suggest that the relief has been as dramatic as today since ≥ 5 Ma, but more data are required to fully investigate this hypothesis.

Exhumation rate decrease around 15 Ma revealed by the simulations of the vertical profile could be attributed to various processes. Post-emplacement thermal re-equilibration of the Bergell pluton is unlikely, considering the closure temperature of the AHe system and the intrusion depth of the pluton (20-26 km, Davidson al., 1996). Contrasted or evolving topography could also induce isotherm deflection (Braun, 2002). As the total horizontal distance between our samples is small (~6 km) such an effect should be negligible, even if

the imperfect fit of the model to the data may indicate local isotherm perturbation. Finally, the most likely interpretation is that the exhumation rate decrease aronud ~15 Ma is related with the Bergell unroofing resulting from the interaction of local uplift and erosion. Based on AHe, Zircon He and AFT ages of boulders from the Bergell granite found in the Oligo-Miocene Gonfolite detrital formation in the Po plain, Malusà et al. (2011) suggest a 1.3 to 1.4 km/Myr exhumation rate of the Bergell massif from ~25 to ~18-16 Ma (Fig. 6). Our simulations of both AHe and AFT data suggest exhumation rate of 0.3 to 0.5 km/Myr between ~17 and ~15 Ma. This implies a significant decrease at ~17 Ma. Such a decrease is contemporaneous with the end of the main dextral strike-slip motion along the Tonale Fault linked to the activation of the Giudicarie fault (Ciancaleoni & Marquer, 2008, Fig. 6). At that time, upper crustal thrusting due to the Adriatic lower crustal indentation (Schmid et al., 1996; Rosenber & Berger, 2009) migrated to the Southern Alps initiating the Lombardic deformation phase that lasted to Messinian time (7.1 – 5.3 Ma) (Fig. 6) (Pieri & Groppi, 1981; Schumacher et al., 1996; Fantoni et al., 2001). Such evolution most likely controlled the decrease of the Bergell exhumation rate around 17-15 Ma.

Modeling results also suggest that exhumation rates increased sometime after 5-6 Ma (0.2 to 0.5 mm/yr) after having reached a minimal value at ~10 Ma (≤0.1 km/Myr). At that time, local deformation was over (see above) and this increase is more likely controlled by external factors. Post 5-6 Ma increase of exhumation rate has been observed in various localities in the Alps and inferred for the whole orogen (e.g. Kuhlemann et al., 2002; Cederbom et al., 2004). This increase is either interpreted as related to climate change around 3-5 Ma (Cederbom et al., 2004; Willett et al., 2006), Messinian base level drop at ~6 Ma (Krijgsman et al., 2002) or intensification of glaciations around 0.87 Ma (Muttoni et al., 2003). Our results, suggest that the increase took place close to 5-6 Ma which rather suggest a Messinian event (Fig. 6). Actually, the Bergell massif is located close to the Italian great lakes where initial carving has been related with Messinian base level drop (Bini et al., 1978, Preusser et al., 2010). However, our interpretation is based on the thermal model as no ages younger than 5.4 Ma have been obtained and further thermochronological work is required to fully investigate the post 5-6 Ma exhumation.

CONCLUSION

The Bergell pluton shows a complex Miocene exhumation history. Following Oligocene emplacement (32-28 Ma), a first exhumation event is related with backthrusting along the Insubric mylonitic belt until ~25 Ma, and continues until ~17 Ma during dextral motion on the Tonale fault (e.g. Ciancaleoni &

Marquer, 2008; Malusà et al., 2011) (Fig. 6). A decrease of the Bergell exhumation rate after ~17 Ma is most likely linked with the southward migration of the thrusts (Lombardic phase, Fig. 6, Rosenber & Berger, 2009). The slow exhumation episode around 10-6 Ma might correspond with the end of this tectonic event (Fig. 6). Our modeling also suggests that exhumation rate increases after 5-6 Ma probably driven by external forcing (Fig. 6).

Acknowledgements

Rosella Pinna is warmly thanks for the U and Th determination of the samples. This work has been financially supported by the ANR-06-JCJC-0079 "Jeune-chercheur 2006" project of Cécile Gautheron. We thank Frederic Herman and Sean Willet for fruitful discussions that helped improving this manuscript. The three anonymous reviewers are thanked for their constructive comments.

References

Bini, A., Cita, M.B. and Gaetani, M., 1978. Southern Alpine Lakes - Hypothesis of an Erosional Origin Related to Messinian Entrenchment *Marine Geology*, **27**, 271-288.

Braun, J., 2002. Quantifying the effect of recent relief changes on age-elevation relationships *Earth and Planetary Science Letters*, **200**, 331-343.

Braun, J. and Robert, X., 2005. Constraints on the rate of post-orogenic erosional decay from low-temperature thermochronological data: application to the Dabie Shan, China *Earth Surface Processes and Landforms*, **30**, 1203-1225.

Cederbom, C.E., Sinclair, H.D., Schlunegger, F. and Rahn, M.K., 2004. Climate-induced rebound and exhumation of the European Alps *Geology*, **32**, 709-712.

Ciancaleoni, L. and Marquer, D., 2008. Late Oligocene to early Miocene lateral extrusion at the eastern border of the Lepontine dome of the central Alps (Bergell and Insubric areas, eastern central Alps) *Tectonics*, **27**, -.

Davidson, C., Rosenberg, C. and Schmid, S.M., 1996. Synmagmatic folding of the base of the Bergell pluton, Central Alps *Tectonophysics*, **265**, 213-238.

Di Giulio, A., Carrapa, B., Fantoni, R., et al., 2001. Middle Eocene to Early Miocene sedimentary evolution of the western Lombardian segment of the South Alpine foredeep (Italy) *International Journal of Earth Sciences*, **90**, 534-548.

Dodson, M.H., 1973. Closure Temperature in Cooling Geochronological and Petrological Systems *Contributions to Mineralogy and Petrology*, **40**, 259-274.

Engi, M., Bousquet, R. and Berger, A., 2004. Explanatory notes to the map: metamorphic structure of the Alps, Central Alps *Mitteilungen der Österreichischen Mineralogischen Gesellschaft*, **149**, 157-173.

Evans, N.J., Byrne, J.P., Keegan, J.T. and Dotter, L.E., 2005. Determination of uranium and thorium in zircon, apatite, and fluorite: Application to laser (U-Th)/He thermochronology *Journal of Analytical Chemistry*, **60**, 1159-1165.

Farley, K.A., 2000. Helium diffusion from apatite: General behavior as illustrated by Durango fluorapatite *Journal of Geophysical Research-Solid Earth*, **105**, 2903-2914.

Farley, K.A., 2002. (U-Th)/He dating: Techniques, calibrations, and applications *Noble Gases in Geochemistry and Cosmochemistry*, **47**, 819-844.

Fellin, M.G., Reiners, P.W., Brandon, M.T., et al., 2007. Thermochronologic evidence for the exhumational history of the Alpi Apuane metamorphic core complex, northern Apennines, Italy *Tectonics*, **26**.

Fox, M., Herman, F. and Willett, S.D., in prep. Inferring exhumation rates in space and time from spatially distributed thermochronological data.

Gautheron, C., Tassan-Got, L., Barbarand, J. and Pagel, M., 2009. Effect of alpha-damage annealing on apatite (U-Th)/He thermochronology *Chemical Geology*, **266**, 166-179.

Gautheron, C.E., Tassan-Got, L. and Farley, K.A., 2006. (U-Th)/Ne chronometry *Earth and Planetary Science Letters*, **243**, 520-535.

Hurford, A.J., 1986. Cooling and Uplift Patterns in the Lepontine Alps South Central Switzerland and an Age of Vertical Movement on the Insubric Fault Line *Contributions to Mineralogy and Petrology*, **92**, 413-427.

Ketcham, R.A., Carter, A., Donelick, R.A., et al., 2007. Improved modeling of fission-track annealing in apatite *American Mineralogist*, **92**, 799-810.

Kraml, M., Pik, R., Rahn, M., et al., 2006. A new multi-mineral age reference material for Ar-40/Ar-39, (U-Th)/He and fission track dating methods: The Limberg t3 tuff *Geostandards and Geoanalytical Research*, **30**, 73-86.

Krijgsman, W., Blanc-Valleron, M.M., Flecker, R., et al., 2002. The onset of the Messinian salinity crisis in the Eastern Mediterranean (Pissouri Basin, cyprus) *Earth and Planetary Science Letters*, **194**, 299-310.

Kuhlemann, J., Frisch, W., Szekely, B., et al., 2002. Post-collisional sediment budget history of the Alps: tectonic versus climatic control *International Journal of Earth Sciences*, **91**, 818-837.

Malusa, M.G., Villa, I.M., Vezzoli, G. and Garzanti, E., 2011. Detrital geochronology of unroofing magmatic complexes and the slow erosion of Oligocene volcanoes in the Alps *Earth and Planetary Science Letters*, **301**, 324-336.

Mancktelow, N.S. and Grasemann, B., 1997. Time-dependent effects of heat advection and topography on cooling histories during erosion *Tectonophysics*, **270**, 167-195.

McDowell, F.W., McIntosh, W.C. and Farley, K.A., 2005. A precise Ar-40-Ar-39 reference age for the Durango apatite (U-Th)/He and fission-track dating standard *Chemical Geology*, **214**, 249-263.

Muttoni, G., Carcano, C., Garzanti, E., et al., 2003. Onset of major Pleistocene glaciations in the Alps *Geology*, **31**, 989-992.

Oberli, F., Meier, M., Berger, A., et al., 2004. U-Th-Pb and Th-230/U-238 disequilibrium isotope systematics: Precise accessory mineral chronology and melt evolution tracing in the Alpine Bergell intrusion *Geochimica Et Cosmochimica Acta*, **68**, 2543-2560.

Pieri, M. and Groppi, G., 1981. Subsurface geological structure of the Po Plain: *CNR, Pubblicazione del Progetto Finalizzato Geodinamica*, **414**, 23.

Preusser, F., Reitner, J.M. and Schluchter, C., 2010. Distribution, geometry, age and origin of overdeepened valleys and basins in the Alps and their foreland *Swiss Journal of Geosciences*, **103**, 407-426.

Ratschbacher, L., Merle, O., Davy, P. and Cobbold, P., 1991. Lateral Extrusion in the Eastern Alps.1. Boundary-Conditions and Experiments Scaled for Gravity *Tectonics*, **10**, 245-256.

Reiners, P.W., Zhou, Z.Y., Ehlers, T.A., et al., 2003. Post-orogenic evolution of the Dabie Shan, eastern China, from (U-Th)/He and fission-track thermochronology *American Journal of Science*, **303**, 489-518.

Rosenberg, C.L. and Berger, A., 2009. On the causes and modes of exhumation and lateral growth of the Alps *Tectonics*, **28**.

Rosenberg, C.L., Berger, A. and Schmid, S.M., 1995. Observations from the Floor of a Granitoid Pluton - Inferences on the Driving-Force of Final Emplacement *Geology*, **23**, 443-446.

Rosenberg, C.L. and Heller, F., 1997. Tilting of the Bergell Pluton and central Lepontine area: Combined evidence from paleomagnetic, structural and petrological data *Eclogae Geologicae Helvetiae*, **90**, 345-356.

Schlunegger, F., Burbank, D.W., Matter, A., et al., 1996. Magnetostratigraphic calibration of the Oligocence to Middle Miocene (30-15 Ma) mammal biozones and depositional sequences of the Swiss Molasse basin *Eclogae Geologicae Helvetiae*, **89**, 753-788.

Schmid, S.M., Fugenschuh, B., Kissling, E. and Schuster, R., 2004. Tectonic map and overall architecture of the Alpine orogen *Eclogae Geologicae Helvetiae*, **97**, 93-117.

Schmid, S.M., Pfiffner, O.A., Froitzheim, N., et al., 1996. Geophysical-geological transect and tectonic evolution of the Swiss-Italian Alps *Tectonics*, **15**, 1036-1064.

Schumacher, M.E. and Laubscher, H.P., 1996. 3D crustal architecture of the Alps-Apennines join - A new view on seismic data *Tectonophysics*, **260**, 349-363.

Stuwe, K., White, L. and Brown, R., 1994. The Influence of Eroding Topography on Steady-State Isotherms - Application to Fission-Track Analysis *Earth and Planetary Science Letters*, **124**, 63-74.

Tapponnier, P., Peltze, G. and Armijo, R., 1986. On the mechanics of the collision between India and Asia. *In "Collision tectonics', edited by Coward and A.C. Riess. Geol. Soc. Spec. Pub., London*, **19**, 115-157.

Tarantola, A., *Inverse Problem Theory and Methods for Model Parameter Estimation*. SIAM.

Thomson, S.N., Brandon, M.T., Reiners, P.W., et al., 2010. Thermochronologic evidence for orogen-parallel variability in wedge kinematics during extending convergent orogenesis of the northern Apennines, Italy *Geological Society of America Bulletin*, **122**, 1160-1179.

Villa, I.M. and von Blanckenburg, F., 1991. A Hornblende 39Ar-40Ar traverse of the Bregaglia tonalite (southeast centra Alps) *Schweizerische Mineralogische Und Petrographische Mitteilungen*, **71**, 73-87.

Wagner, G.A., Miller, D.S. and Jager, E., 1979. Fission-Track Ages on Apatite of Bergell Rocks from Central Alps and Bergell Boulders in Oligocene Sediments *Earth and Planetary Science Letters*, **45**, 355-360.

Wagner, G.A., Reimer, G.M. and Jäger, E., 1977. Cooling ages derived by apatite fission-track, mica Rb-Sr and K-Ar dating: the uplift and cooling history of the Central Alps *Memory of the Institude of geology and Mineralogy University of Padova*.

Willett, S.D., Schlunegger, F. and Picotti, V., 2006. Messinian climate change and erosional destruction of the central European Alps *Geology*, **34**, 613-616.

Zachos, J., Pagani, M., Sloan, L., et al., 2001. Trends, rhythms, and aberrations in global climate 65 Ma to present *Science*, **292**, 686-693.

Zhang, P.Z., Molnar, P. and Downs, W.R., 2001. Increased sedimentation rates and grain sizes 2-4 Myr ago due to the influence of climate change on erosion rates *Nature*, **410**, 891-897.

Zwingmann, H. and Mancktelow, N., 2004. Timing of Alpine fault gouges *Earth and Planetary Science Letters*, **223**, 415-425.

Figure caption:

Figure 1: Geological, tectonic and morphologic setting of the Bergell area and samples location. (a) location of the studied area (black frame corresponding to Fig. 1b) within the western Alps (ETOPO shaded relief). GF: Giudicarie fault, TF: Tonale fault, SF: Simplon fault, PF: Pennic Front, EL: Engadine Line, AFT: Alpine frontal trust. (b) Structural map of the studied area After Schmid et al. (2004) and Ciancaleoni & Marquer (2008), with samples location and corresponding ages. (c) Landsat image showing the morphology of the central and highest part of the Bergell massif (black frame on Fig. 1b).

Figure 2: Topographic profiles across the Bergell area and AHe ages. (a and b) swath profiles with maximum and minimum elevations (location on Fig. 1b) and projected samples location (circles, black when projected from outside of the swath). Elevation data from ASTER digital elevation model (ASTER GDEM is a product of METI and NASA). (a) S-N profile. (b) WSW-ENE profile.

Figure 3: AHe (white circles) and AFT (black circles) ages of the Bergell vertical profile (see location on Fig 1b and 2b) plotted with respect to elevation. AFT data from Wagner et al. (1977; 1979).

Figure 4: SEM images of apatite grains representative of those used for AHe dating.

Figure 5: Results of thermal modelling of the Bergell exhumation history for various prior exhumation rates and initial geothermal gradients. The grey envelope illustrates one standard deviation from the mean solution shown as a solid black line.

Figure 6: Chronology of the main of Bergell exhumation phases and main known tectonic and climatic events. (1) This study; (2) Malusà et al., 2011; (3) Hurford (1986); Schmid et al. (1996); (4) Ciancaleoni & Marquer (20008); (5) Pieri & Groppi (1981); Schumacher et al. (1996); Fantoni et al. (2001) ; (6) Pieri & Groppi (1981); Willet et al. (2006); (7) Krijgsman et al. (2002); Schlunegger et al. (1996); Zachos et al. (2001); (9) Zhang et al. (2001); (10) Muttoni et al. (2003).

Table 1: Sample details and analytical (U-Th)/He data. For all other samples four apatites grains have been analyzed per replicate (n: number of used grains). * indicates datum not taken into account into the mean age calculation. The replicate error is the analytical errors. The mean error is taken as the standard deviation of the replicate age. F_T: He ejection correction factor.

Table 1:

Sample name	UTM (32) Northing	UTM (32) Easting	Elevation (m)	n	F_T	Weight (ng)	^{4}He (nmol/g)	U (ppm)	Th (ppm)	Th/U	Raw Age (Ma)	Error (1σ)	F_T corrected Age (Ma)	Error (1σ)
BG01_A				4	0.70	7.73	0.83	17.68	23.08	1.31	6.7	0.5	9.5	1.1
BG01_B				4	0.73	8.57	0.67	17.05	15.47	0.91	6.0	0.4	8.2	1.0
BG01_C				4	0.76	13.97	0.82	15.10	16.44	1.09	8.0	0.5	10.5	1.2
BG01_D				4	0.67	5.77	0.97	21.59	24.97	1.16	6.6	0.4	9.8	1.2
BG01	**535189**	**5112943**	**1040**								**Mean age**		**9.5**	**1.0**
Tonalite														
BG03_A				1	0.74	2.85	0.46	7.93	12.56	1.58	7.8	0.8	10.6	1.6
BG03_B				1	0.74	2.85	0.39	3.89	13.23	3.40	10.4	1.3	14.1	2.4
BG03_C				4	0.72	6.21	0.42	4.83	14.73	3.05	9.4	0.8	13.1	1.7
BG03_D				4	0.71	5.76	0.42	10.16	8.18	0.81	6.5	0.5	9.1	1.2
BG03_E				4	0.70	5.23	0.36	6.19	11.01	1.78	7.5	0.7	10.8	1.5
BG03	**560116**	**5114729**	**1091**								**Mean age**		**11.5**	**2.0**
Migmatitic orthogneiss														
BG06_A				4	0.73	7.16	1.43	23.94	31.62	1.32	8.4	0.6	11.6	1.3
BG06_B				4	0.72	8.60	1.26	27.88	24.79	0.89	6.9	0.4	9.6	1.1
BG06_C				4	0.75	8.52	0.72	13.20	16.85	1.28	7.8	0.5	10.4	0.7
BG06_D				4	0.73	9.04	0.97	22.27	20.64	0.93	6.6	0.4	9.1	1.0
BG06	**564161**	**5114511**	**1082**								**Mean age**		**10.1**	**1.1**
Granodiorite														
BG17_A				4	0.75	11.77	7.37	91.15	60.77	0.67	12.9	0.8	17.2	1.9
BG17_B				4	0.80	19.49	7.84	104.57	56.69	0.54	12.3	0.7	15.4	0.9
BG17_C				4	0.75	9.29	6.62	90.74	52.84	0.58	11.9	0.7	15.8	1.0
BG17_D				4	0.77	11.77	24.30	121.60	77.97	0.64	32.2	2.0	*41.8**	*2.5*
BG17	**544727**	**5126618**	**3137**								**Mean age**		**16.2**	**1.0**
Granodiorite														
BG21_A				4	0.66	5.91	8.19	140.52	69.92	0.50	9.7	0.6	14.6	0.9
BG21_B				4	0.77	11.88	2.09	117.76	58.01	0.49	2.9	0.2	*3.8**	*0.4*
BG21_C				4	0.72	12.06	5.11	72.69	38.23	0.53	11.6	0.7	16.1	1.0
BG21_D				4	0.73	8.16	8.14	130.43	65.25	0.50	10.3	0.6	14.2	0.9
BG21	**545306**	**5124168**	**2048**								**Mean age**		**15.0**	**1.0**
Tonalite														
BG23_A				4	0.75	6.62	7.89	153.82	64.61	0.42	8.6	0.5	11.5	0.7
BG23_B				4	0.76	10.10	6.88	133.45	88.64	0.66	8.3	0.5	10.9	0.7
BG23_C				4	0.76	13.88	6.79	138.60	65.04	0.47	8.2	0.5	10.7	0.7
BG23_D				4	0.74	10.12	8.94	160.87	85.80	0.53	9.1	0.6	12.4	0.8
BG23	**545730**	**5122878**	**1702**								**Mean age**		**11.4**	**0.7**
Granodiorite														
BG25_A				4	0.73	5.71	0.93	26.02	5.43	0.21	6.3	0.4	8.7	0.6
BG25_B				4	0.73	7.87	0.84	23.95	4.56	0.19	6.2	0.4	8.6	0.6
BG25_C				4	0.72	7.01	0.81	25.39	4.00	0.16	5.7	0.4	7.9	0.5
BG25_D				5	0.67	5.50	1.03	28.71	6.11	0.21	6.3	0.4	9.5	0.7
BG25	**545693**	**5121730**	**1236**								**Mean age**		**8.7**	**0.6**
Basic migmatite														
BG26_A				4	0.78	13.04	2.80	112.08	49.00	0.44	4.2	0.3	5.4	0.3
BG26_B				4	0.74	5.91	3.55	140.46	65.38	0.47	4.2	0.3	5.7	0.4
BG26_D				4	0.72	8.22	2.63	115.77	56.42	0.49	3.8	0.2	5.2	0.3
BG26	**547229**	**5121074**	**1039**								**Mean age**		**5.4**	**0.2**
Granodiorite														
BG27_A				4	0.76	11.51	3.10	103.07	66.45	0.64	4.8	0.3	6.4	0.4
BG27_B				4	0.74	9.74	2.91	97.94	68.31	0.70	4.7	0.3	6.4	0.4
BG27-C				4	0.74	12.20	2.61	84.98	58.16	0.68	4.9	0.3	6.6	0.4
BG27_D				4	0.74	10.88	2.25	77.96	40.57	0.52	4.8	0.3	6.4	0.4
BG27	**548771**	**5118362**	**1024**								**Mean age**		**6.5**	**0.1**
Granodiorite														
BG40_A				1	0.75	3.17	0.42	8.11	37.13	4.58	4.6	0.4	6.1	0.5
BG40_B				1	0.66	1.32	0.57	27.95	11.06	0.40	3.5	0.3	5.2	0.5
BG40_C				1	0.73	2.29	2.03	71.00	52.75	0.74	4.5	0.3	6.2	0.4
BG40	**542442**	**5100394**	**1124**								**Mean age**		**5.8**	**0.5**
Muscovite bearing gneiss														
BG43a_B				1	0.72	2.20	1.01	11.22	95.18	8.48	5.6	0.4	7.7	0.6
BG43a_E				1	0.78	4.35	3.25	75.91	34.25	0.45	7.2	0.5	9.2	0.6
BG43	**506442**	**5112989**	**940**								**Mean age**		**8.5**	**1.0**
Granodiorite														

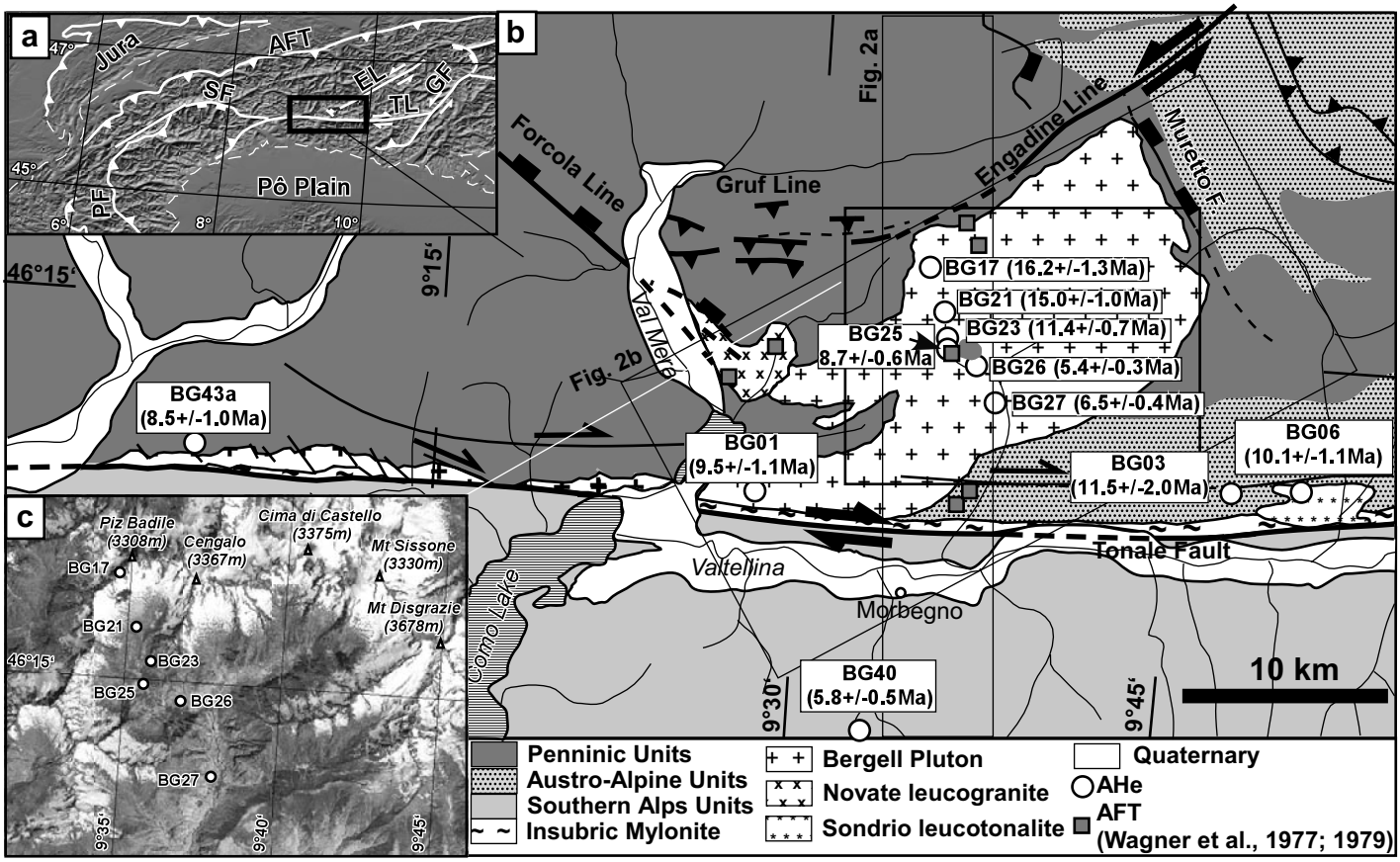
a
Jura
AFT
SF
EL
TL
GF
Pô Plain
PF
47°
45°
6°
8°
10°
b
Fig. 2a
Forcola Line
Gruf Line
Engadine Line
Muretto F.
46°15'
9°15'
Val Mera
Fig. 2b
BG17 (16.2+/-1.3Ma)
BG21 (15.0+/-1.0Ma)
BG23 (11.4+/-0.7Ma)
BG25
8.7+/-0.6Ma
BG26 (5.4+/-0.3Ma)
BG27 (6.5+/-0.4Ma)
BG43a
(8.5+/-1.0Ma)
BG01
(9.5+/-1.1Ma)
BG03
(11.5+/-2.0Ma)
BG06
(10.1+/-1.1Ma)
Tonale Fault
Valtellina
Como Lake
Morbegno
BG40
(5.8+/-0.5Ma)
9°30'
9°45'
10 km
c
Piz Badile
(3308m)
Cengalo
(3367m)
Cima di Castello
(3375m)
Mt Sissone
(3330m)
Mt Disgrazie
(3678m)
BG17
BG21
BG23
BG25
BG26
BG27
46°15'
9°35'
9°40'
9°45'
Penninic Units
Austro-Alpine Units
Southern Alps Units
Insubric Mylonite
Bergell Pluton
Novate leucogranite
Sondrio leucotonalite
Quaternary
AHe
AFT
(Wagner et al., 1977; 1979)

Fig 1

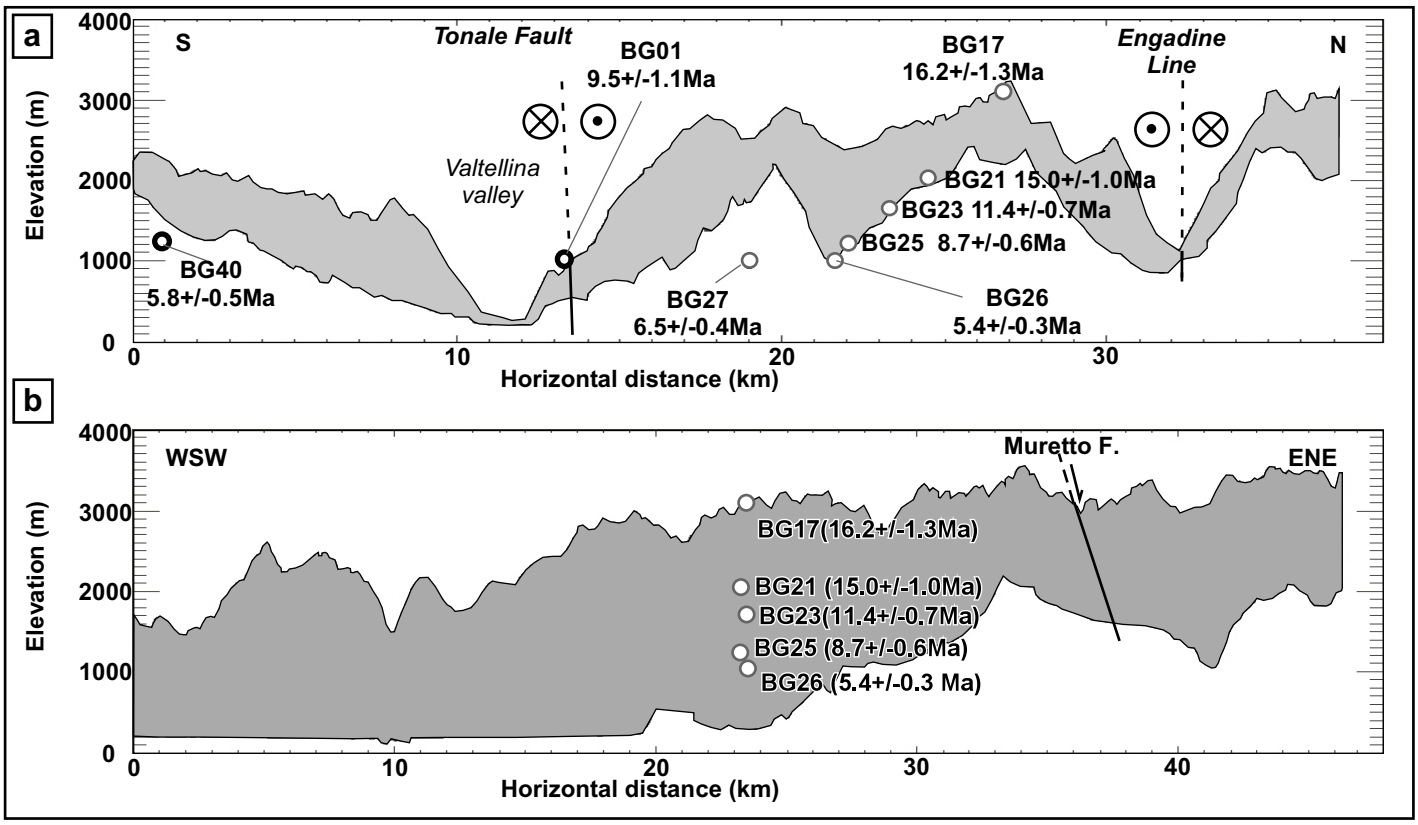
a
S
Tonale Fault
BG01
9.5+/-1.1Ma
BG17
16.2+/-1.3Ma
Engadine
Line
N
Valtellina
valley
BG21 15.0+/-1.0Ma
BG23 11.4+/-0.7Ma
BG25 8.7+/-0.6Ma
BG40
5.8+/-0.5Ma
BG27
6.5+/-0.4Ma
BG26
5.4+/-0.3Ma
Elevation (m)
Horizontal distance (km)
b
WSW
Muretto F.
ENE
BG17(16.2+/-1.3Ma)
BG21 (15.0+/-1.0Ma)
BG23(11.4+/-0.7Ma)
BG25 (8.7+/-0.6Ma)
BG26 (5.4+/-0.3 Ma)
Elevation (m)
Horizontal distance (km)

Figure 2

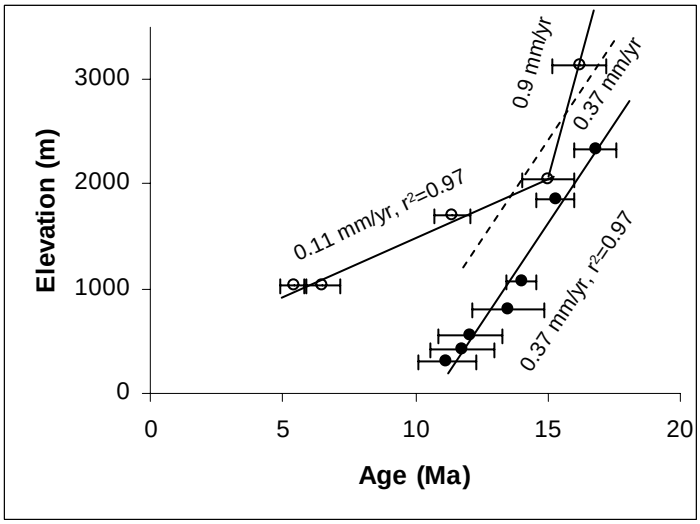
Elevation (m)
3000
2000
1000
0
0
5
10
15
20
Age (Ma)
0.9 mm/yr
0.37 mm/yr
0.11 mm/yr, r2=0.97
0.37 mm/yr, r2=0.97

Figure 3

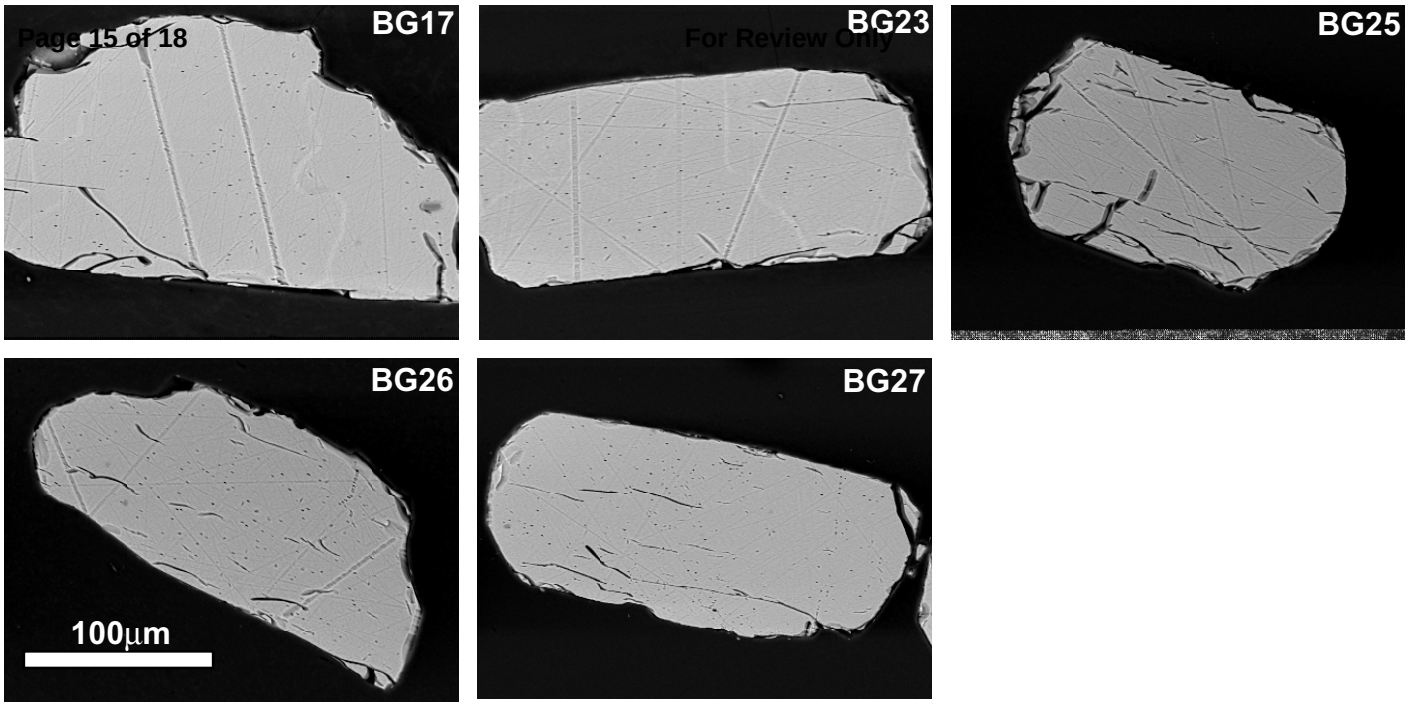

Figure 1

A.
Prior exhumation rate: 0.3 +/- 0.15 mm/yr
Starting geothermal gradient: 35.7 °C/km
Final geothermal gradient: 45.2 °C/km
A priori chi: 13.7
Final chi: 1.6
Time interval: 3 Ma

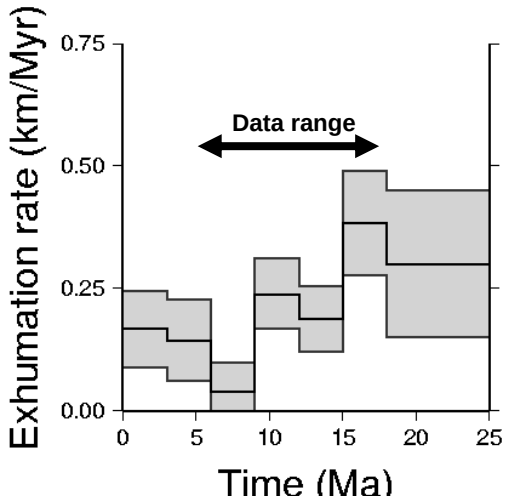

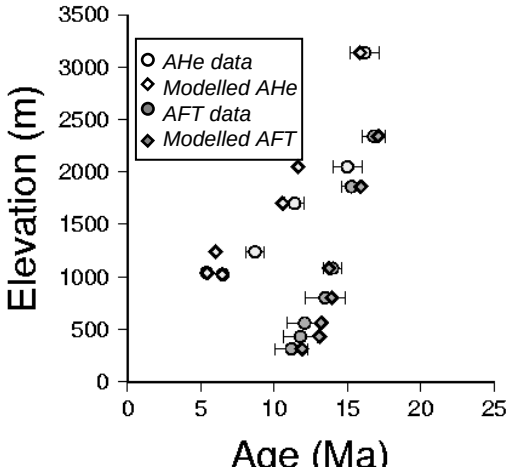

B.
Prior exhumation rate: 0.3 +/- 0.15 mm/yr
Starting geothermal gradient: 32.6°C/km
Final geothermal gradient: 42.3°C/km
A priori chi: 10.7
Final chi: 1.7
Time interval: 3Ma

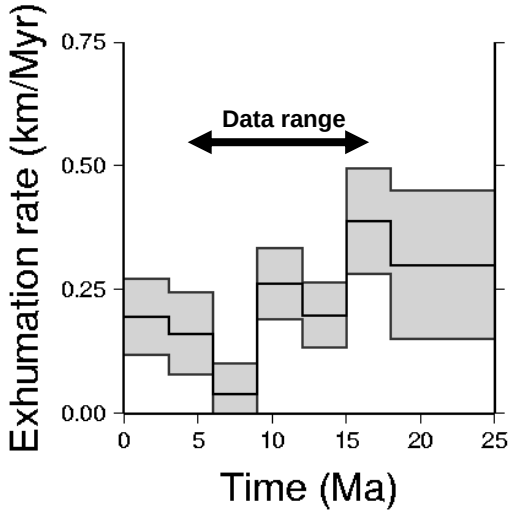

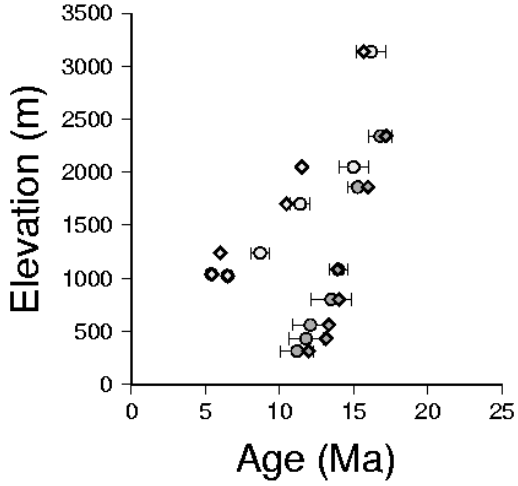

C.
Prior exhumation rate: 0.3 +/- 0.15 mm/yr
Starting geothermal gradient: 24.3°C/km
Final geothermal gradient: 31.5°C/km
A priori chi: 5.3
Final chi: 1.9
Time interval: 3Ma

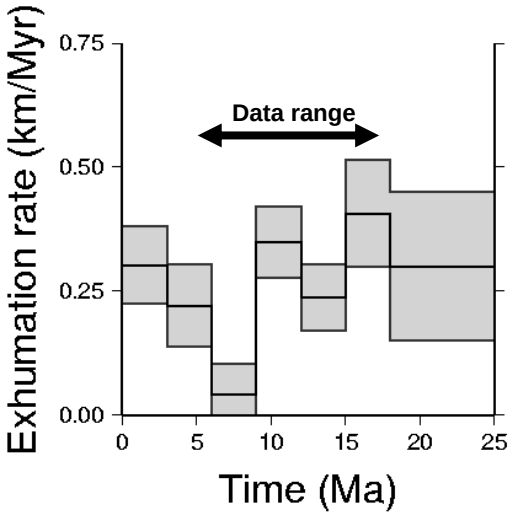

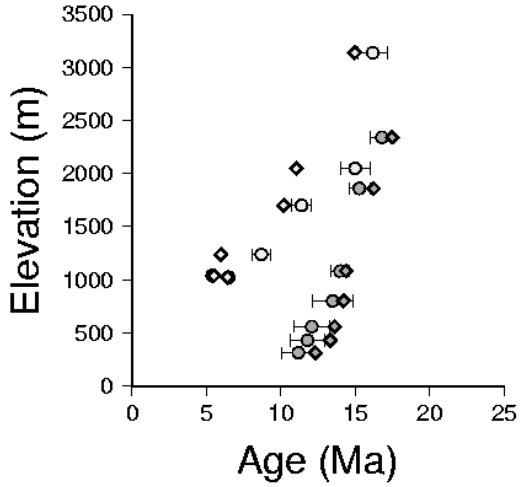

D.
Prior exhumation rate: 0.3 +/- 0.15 mm/yr
Starting geothermal gradient: 16.2 °C/km
Final geothermal gradient: 21.0 °C/km
A priori chi: 7.2
Final chi: 2.4
Time interval 3 Ma

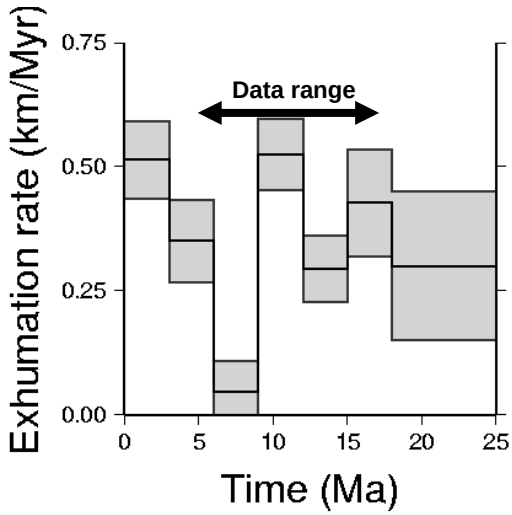

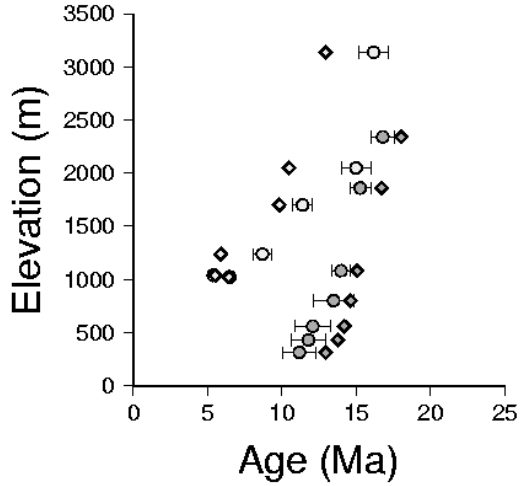

E.
Prior exhumation rate: 0.5 +/- 0.15 mm/yr
Starting geothermal gradient: 24.4°C/km
Final geothermal gradient: 37.5°C/km
A priori chi: 14.1
Final chi: 1.7
Time interval: 3Ma

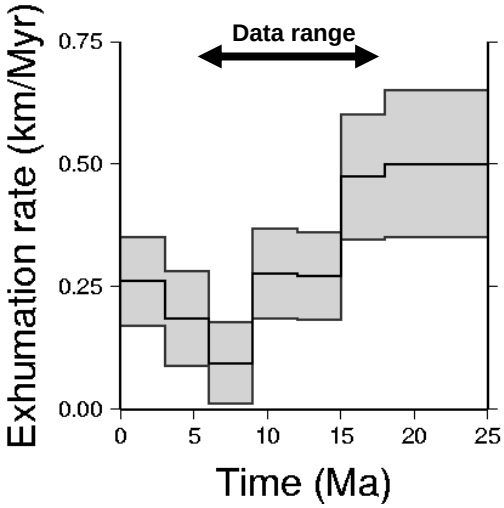

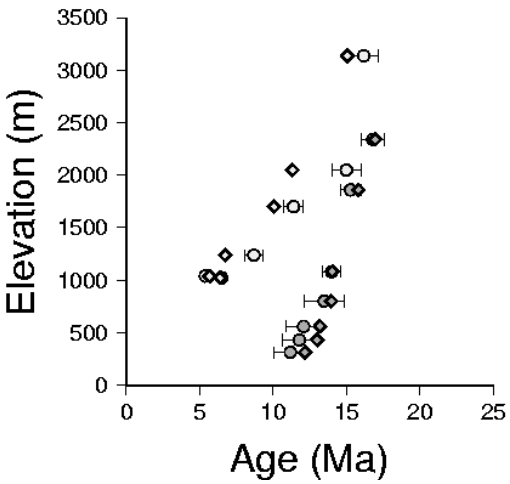

F.
Prior exhumation rate: 0.5 +/- 0.15 mm/yr
Starting geothermal gradient: 24.4 °C/km
Final geothermal gradient: 37.5°C/km
A priori chi: 14.1
Final chi: 1.6
Time interval: 5Ma

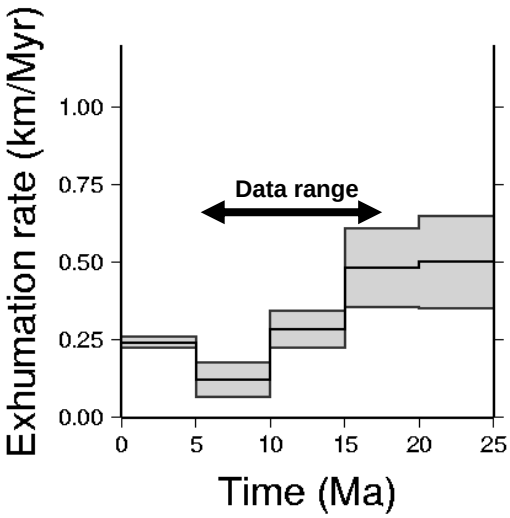

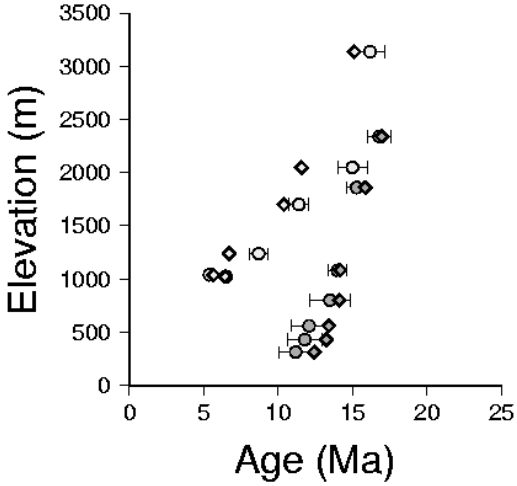

H.
Prior exhumation rate: 1.0 +/- 0.15 mm/yr
Starting geothermal gradient: 16.3 °C/km
Final geothermal gradient: 37.0°C/km
A priori chi: 18.4
Final chi: 2.4
Time interval: 3Ma

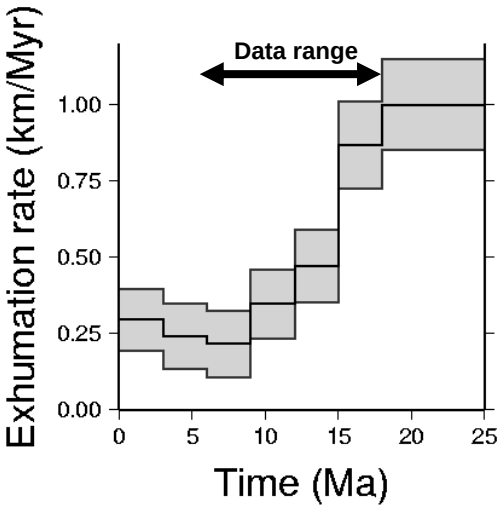

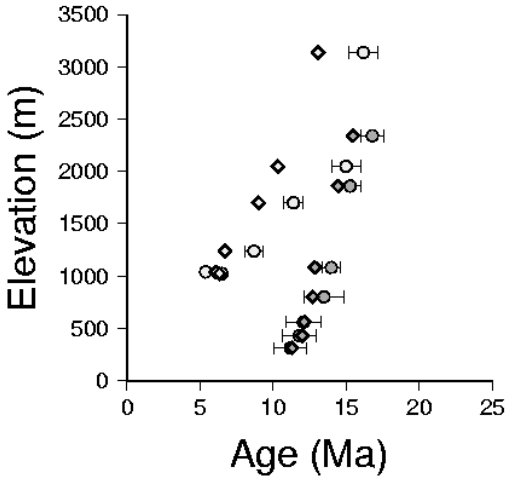

G.
Prior exhumation rate: 0.7 +/- 0.15 mm/yr
Starting geothermal gradient: 19.5°C/km
Final geothermal gradient: 35.3°C/km
A priori chi: 16.0
Final chi: 1.9
Time interval: 3Ma

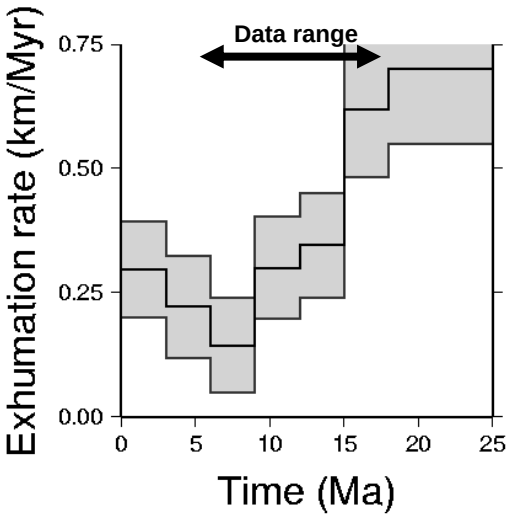

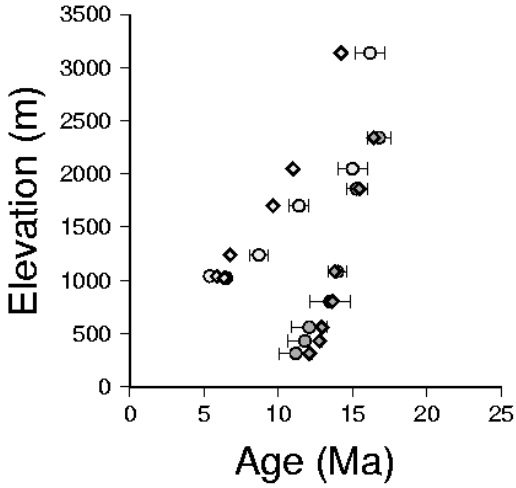

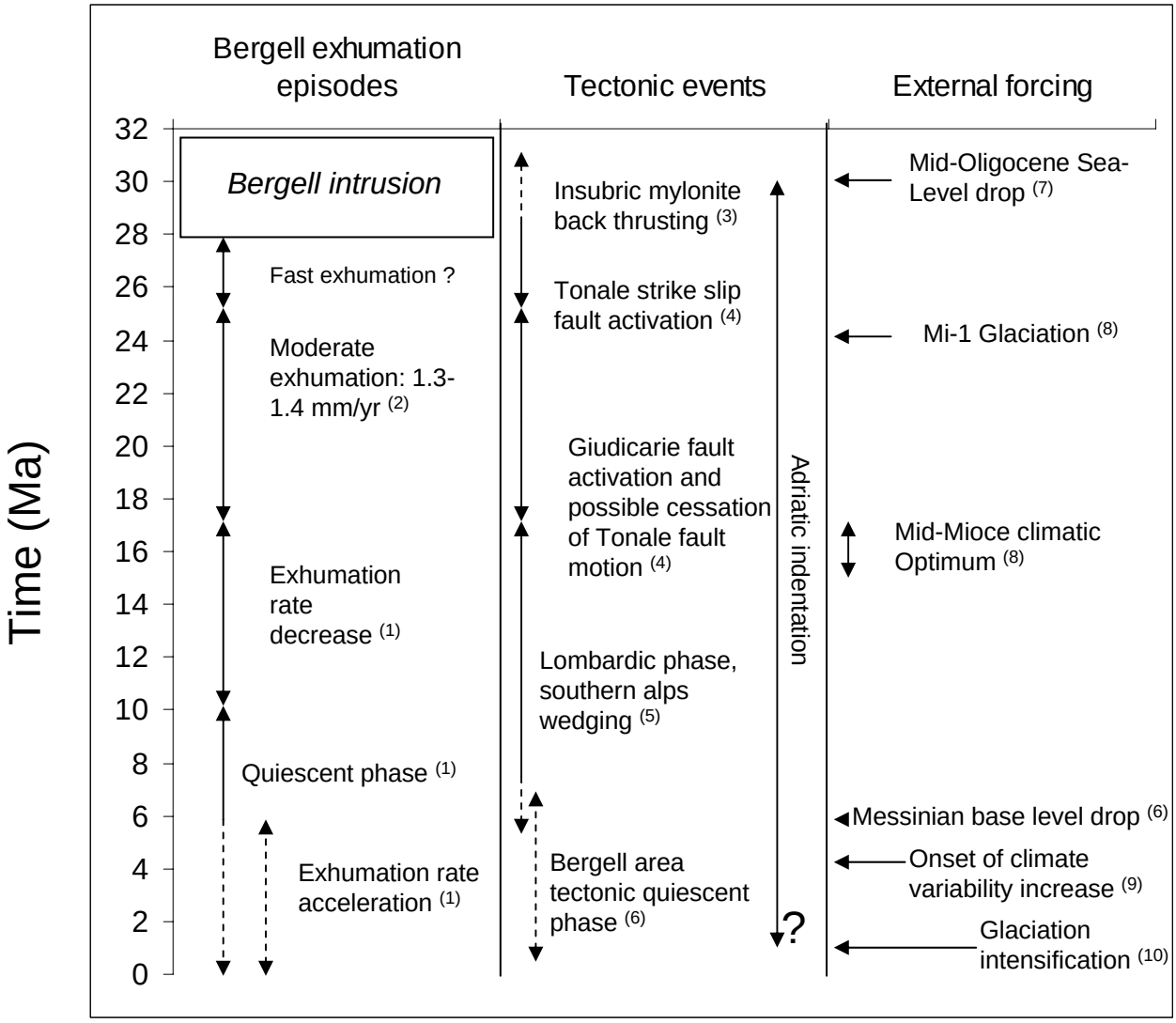
Bergell exhumation episodes
Tectonic events
External forcing
Time (Ma)
32
30
28
26
24
22
20
18
16
14
12
10
8
6
4
2
0
Bergell intrusion
Fast exhumation ?
Moderate exhumation: 1.3-1.4 mm/yr (2)
Exhumation rate decrease (1)
Quiescent phase (1)
Exhumation rate acceleration (1)
Insubric mylonite back thrusting (3)
Tonale strike slip fault activation (4)
Giudicarie fault activation and possible cessation of Tonale fault motion (4)
Lombardic phase, southern alps wedging (5)
Bergell area tectonic quiescent phase (6)
Adriatic indentation
?
Mid-Oligocene Sea-Level drop (7)
Mi-1 Glaciation (8)
Mid-Mioce climatic Optimum (8)
Messinian base level drop (6)
Onset of climate variability increase (9)
Glaciation intensification (10)

Figure 6